OPEN ACCESS



Return Currents in Collisionless Shocks

Siddhartha Gupta^{1,2}, Damiano Caprioli^{1,3}, and Anatoly Spitkovsky² Department of Astronomy and Astrophysics, The University of Chicago, IL 60637, USA; gsiddhartha@princeton.edu

Department of Astrophysical Sciences, Princeton University, 4 Ivy Ln., Princeton, NJ 08544, USA

Brico Fermi Institute, The University of Chicago, Chicago, IL 60637, USA

Received 2023 December 12; revised 2024 April 11; accepted 2024 April 13; published 2024 June 5

Abstract

Collisionless shocks tend to send charged particles into the upstream, driving electric currents through the plasma. Using kinetic particle-in-cell simulations, we investigate how the background thermal plasma neutralizes such currents in the upstream of quasi-parallel non-relativistic electron-proton shocks. We observe distinct processes in different regions: the far upstream, the shock precursor, and the shock foot. In the far upstream, the current is carried by nonthermal protons, which drive electrostatic modes and produce suprathermal electrons that move toward upstream infinity. Closer to the shock (in the precursor), both the current density and the momentum flux of the beam increase, which leads to electromagnetic streaming instabilities that contribute to the thermalization of suprathermal electrons. At the shock foot, these electrons are exposed to shock-reflected protons, resulting in a two-stream type instability. We analyze these processes and the resulting heating through particle tracking and controlled simulations. In particular, we show that the instability at the shock foot can make the effective thermal speed of electrons comparable to the drift speed of the reflected protons. These findings are important for understanding both the magnetic field amplification and the processes that may lead to the injection of suprathermal electrons into diffusive shock acceleration.

Unified Astronomy Thesaurus concepts: Plasma astrophysics (1261); High energy astrophysics (739); Cosmic rays (329); Magnetic fields (994); Shocks (2086); Plasma physics (2089)

1. Introduction

Energetic charged particles (henceforth cosmic rays—CRs) are the prime sources of γ -ray, X-ray, and radio emission across the universe. Explanation of the acceleration of these particles in shock-powered environments typically relies on the diffusive shock acceleration (DSA) mechanism (e.g., Axford et al. 1977; Bell 1978; Blandford & Ostriker 1978), where the back-reaction from the streaming suprathermal (ST) and/or nonthermal (NT) particles on the plasma plays a crucial role (e.g., Bell 2004; Amato & Blasi 2009). While the observations of several sources have already provided evidence of self-generated electromagnetic (EM) turbulence in the shock upstream (see, e.g., Morlino et al. 2010; Wilson et al. 2016), whether and how such turbulence helps electrons to be injected into the DSA process remains a pressing unsolved problem.

The properties of the upstream turbulence crucially depend on the ability of the shock to produce back-streaming (i.e., moving toward upstream infinity) ions/protons or electrons; this process is controlled by the inclination of the magnetic field relative to the shock normal ($\theta_{\rm Bn}$). Depending on $\theta_{\rm Bn}$, two main regimes can be identified: (i) quasi-parallel ($\theta_{\rm Bn} \lesssim 50^{\circ}$) and (ii) oblique/quasi-perpendicular ($\theta_{\rm Bn} \gtrsim 50^{\circ}$) shocks. Quasi-parallel shocks reflect protons efficiently (see, e.g., Giacalone et al. 1993; Caprioli & Spitkovsky 2014a, 2014b; Caprioli et al. 2015), producing a current that drives the resonant/nonresonant streaming instabilities (e.g., Bell 2004; Amato & Blasi 2009; Bell et al. 2013). In (quasi-)perpendicular shocks, instead, the current may be carried by electrons (Guo et al. 2014a, 2014b; Xu et al. 2020; Kumar & Reville 2021),

Original content from this work may be used under the terms of the Creative Commons Attribution 4.0 licence. Any further distribution of this work must maintain attribution to the author(s) and the title of the work, journal citation and DOI.

unless the shock magnetization is sufficiently low, in which case ion injection is possible (Xu et al. 2020; Orusa & Caprioli 2023).

In all cases, the question arises of how the CR currents are neutralized. Current compensation can operate either by the relative drift between thermal protons and electrons in the background plasma or by a set of electrons that travel alongside or in the opposite direction to the current-driving particles, depending on their charge's sign. These assumptions are usually made in any linear theory of streaming instabilities (see, e.g., Amato & Blasi 2009; Gupta et al. 2021). In general, we can expect that, if the electrons react to compensate the imbalance, then they are likely ST, because it is hard to envision different populations of thermal electrons with different drifts. But are these ST electrons produced locally, or are they shock-reflected energetic electrons?

While several recent studies have used kinetic simulations to unravel the processes responsible for electron acceleration at shocks (e.g., Sironi et al. 2013; Guo et al. 2014a; Park et al. 2015; Bohdan et al. 2019; Crumley et al. 2019; Xu et al. 2020; Arbutina & Zeković 2021; Kumar & Reville 2021; Morris et al. 2022; Shalaby et al. 2022), the characterization of return-current electrons has received much less attention, though the generation of ST electrons may be crucial to electron injection, too.

In this paper, we use kinetic particle-in-cell (PIC) simulations to self-consistently study the origin and compensation of currents produced in the shock upstream. We find that current neutralization gives rise to populations of back-streaming ST electrons, which may be then thermalized closer to the shock; the net result is that the electrons impinging on the shock can be much warmer than those far upstream. We outline our shock simulations in Section 2, and present our main results in Sections 3 and 4. In Sections 5 and 6, we design controlled

simulations to detail the processes found in global shock simulation and show that the electron heating in the shock foot is universal. We extend our discussion to quasi-perpendicular shocks in Section 7, and summarize our results in Section 8.

2. Numerical Setup

We use the EM PIC code Tristan-MP (Spitkovsky 2005) to perform simulations of collisionless shocks. The computational domain is quasi-one-dimensional, with 5 cells in the transverse direction (y-axis). Each cell is initialized with an electron-proton plasma, with 200 particles per cell per species; both species have a Maxwell-Boltzmann distribution with a temperature $T_{i,0} = T_{e,0}$ and thermal speeds $v_{th i,e} =$ $\sqrt{k_{\rm B}T_{\rm i,e,0}/m_{\rm i,e}}$ (for ions/protons and electrons, respectively). Grid spacing and time steps are fixed to $\Delta=d_{\rm e}/10$ and $\Delta t = 0.045~\omega_{\rm pe}^{-1}$, where $\omega_{\rm pe} = \sqrt{4\pi n~e^2/m_{\rm e}}$ is the electron plasma frequency and $d_{\rm e} = c/\omega_{\rm pe}$ is the electron skin depth. The proton skin depth is thus $d_i = \sqrt{m_{\rm R}} \ d_{\rm e}$, where $m_{\rm R} = m_i/m_{\rm e}$ is the proton-to-electron mass ratio. As typical in PIC simulations, to save computational resources, we use a reduced mass ratio, $m_R = 100$, though we study how our results depend on $m_{\rm R}$ using controlled simulations. To reduce numerical noise, we filter the current using 32 passes of the digital filter per time step.

The magnetization of the plasma is defined by the Alfvén speed $v_A = B_0/\sqrt{4\pi m_i n_0}$; the initial magnetic field B_0 forms an angle $\theta_{\rm Bn} = \cos^{-1}(B_x/|B_0|) = 30^{\circ}$ with the shock normal and lays in the x-y plane (quasi-parallel shock). The shock is launched using the left boundary of the computational box as a moving reflecting wall. Such a piston moves with velocity $v_{\rm pt} \gg v_{\rm A}$, $v_{\rm th}$ with respect to the background thermal plasma; thus, simulations are in the upstream frame. Finally, the right boundary is open and expands with time, ensuring the box size remains at the minimum necessary to account for backstreaming high-energy particles.

The shock strength is defined by the Alfvénic Mach number $\mathcal{M}_A \equiv v_{sh}/v_A$, and the sonic Mach number $\mathcal{M}_s \equiv v_{sh}/v_{th,i}$, where $v_{sh} = v_{pt}\mathcal{R}/(\mathcal{R}-1)$ and $\mathcal{R} \equiv \rho_2/\rho_1$ is the shock compression. To obtain the shock parameters, we have assumed $\mathcal{R}=4$, as is typical for strong shocks, though the actual value of \mathcal{R} may be larger than 4 (Caprioli et al. 2020; Haggerty & Caprioli 2020). Finally, we introduce $\tilde{p} \equiv |\boldsymbol{p}|/m_i v_{pt}$ as the particle three-momentum, $|\boldsymbol{p}|$, normalized to the momentum of a proton moving with the piston speed (henceforth piston momentum).

3. The Nature of the Return Current

Figure 1 illustrates the main properties of our benchmark shock, with $v_{\rm pt}=0.2c$, $\mathcal{M}_{\rm A}=20$, $\mathcal{M}_{\rm s}=40$. Figure 1(a) shows the plasma density profile, with the red line marking the shock location at $t=85~\omega_{\rm ci}^{-1}$; the region right (left) of this line represents upstream (downstream). Figure 1(b) displays the profile of the x-component of the plasma velocity (left axis, black curve) and the local inclination of the magnetic field relative to the shock normal (right axis, cyan). Close to the shock, $\theta_{\rm Bn}$ can deviate significantly from 30°, due to the magnetic field amplification driven by the current in backstreaming energetic protons (e.g., Bell 2004; Riquelme & Spitkovsky 2009; Caprioli & Spitkovsky 2014b; Park et al. 2015).

Figures 1(c1) and (c2) show the phase-space distribution f(x, p) of protons and electrons, respectively; their spectra in two regions upstream (marked with red and blue lines in Figures 1(c1) and (c2)) are reported in Figure 1(d). Figures 1(e1) and (e2) show the *x*-component of the particle velocity, $v_x(x, p)$, and Figures 1(f1) and (f2) illustrate the specific current $j_x(x, p)$ carried by protons and electrons with momentum p, which are defined as

$$v_{x}(x,p) \equiv \frac{\int_{p}^{p+\Delta p} u_{x}(x,p') f(x,p') p'^{2} dp'}{\int_{p}^{p+\Delta p} f(x,p') p'^{2} dp'}$$
(1)

$$j_{x}(x, p) = \int_{p}^{p+\Delta p} q \, u_{x}(x, p') f(x, p') p'^{2} dp'. \tag{2}$$

Here, the total momentum p' is measured in the upstream frame, u_x is the x-component of particle's three-velocity, $q=\pm e$ (depending on the species), and Δp is an infinitesimal momentum increment used for estimating distributions. The vertical axes in Figures 1(c1), (c2), (e1), (e2), (f1), and (f2) are normalized to the piston momentum.

Momentum distributions: In Figures 1(c1) and (c2), the golden yellow regions ahead of the shock correspond to the thermal populations. The proton phase space (Figure 1(c1)) contains a population of high-momentum particles ($\tilde{p} \equiv p/m_i v_{\rm pt} \gtrsim 2$) undergoing DSA (hereafter NT, or DSA, protons). The electron phase space (Figure 1(c2)), besides such populations, also contains a third, intermediate, one: electrons with $\tilde{p} \sim 0.01$ (i.e., above their thermal distributions), which we label as suprathermal (ST). These distributions can also be inferred from Figure 1(d), where the red and blue curves represent the spectra between the marked regions of Figures 1(c1), (c2), while black curves represent the initial Maxwell–Boltzmann distribution of the respected species. The origin of such ST electrons is investigated in this paper.

Velocity distributions: The x-p phase-space distribution of v_x (Equation (1)) for each species is shown in Figures 1(e1) and (e2). While far-upstream thermal protons and electrons are at rest, close to the shock they acquire finite velocities to compensate for the currents of back-streaming energetic particles (both NT protons and ST electrons).

Current distributions: Figures 1(f1) and (f2) show the currents carried by particles with momentum p (Equation (2)), while Figure 1(g) shows the total currents in protons and electrons (brown and gray curves), integrated above $\tilde{p} = 2$ for NT protons (orange) and above $\tilde{p} = 0.01$ for ST+NT electrons (blue). Close to the shock, the NT proton current j_{xi} is comparable to the ST electron current. This is a nontrivial finding: in the literature, the proton-driven current is usually assumed to be compensated by thermal electrons—a condition that is imposed by hand (Bell 2004; Amato & Blasi 2009); here, instead, we find that the shock naturally develops a population of back-streaming energetic electrons, whose density and drift speed are regulated to compensate the proton current. At a sufficiently large distance upstream, though, where EM turbulence is weak or has not grown yet, the ST electrons travel almost freely and typically faster than NT protons. This implies that, upstream of the back-streaming protons, there must be another, transient, current imbalance, this time driven by escaping ST electrons, which is compensated by the background thermal electrons.

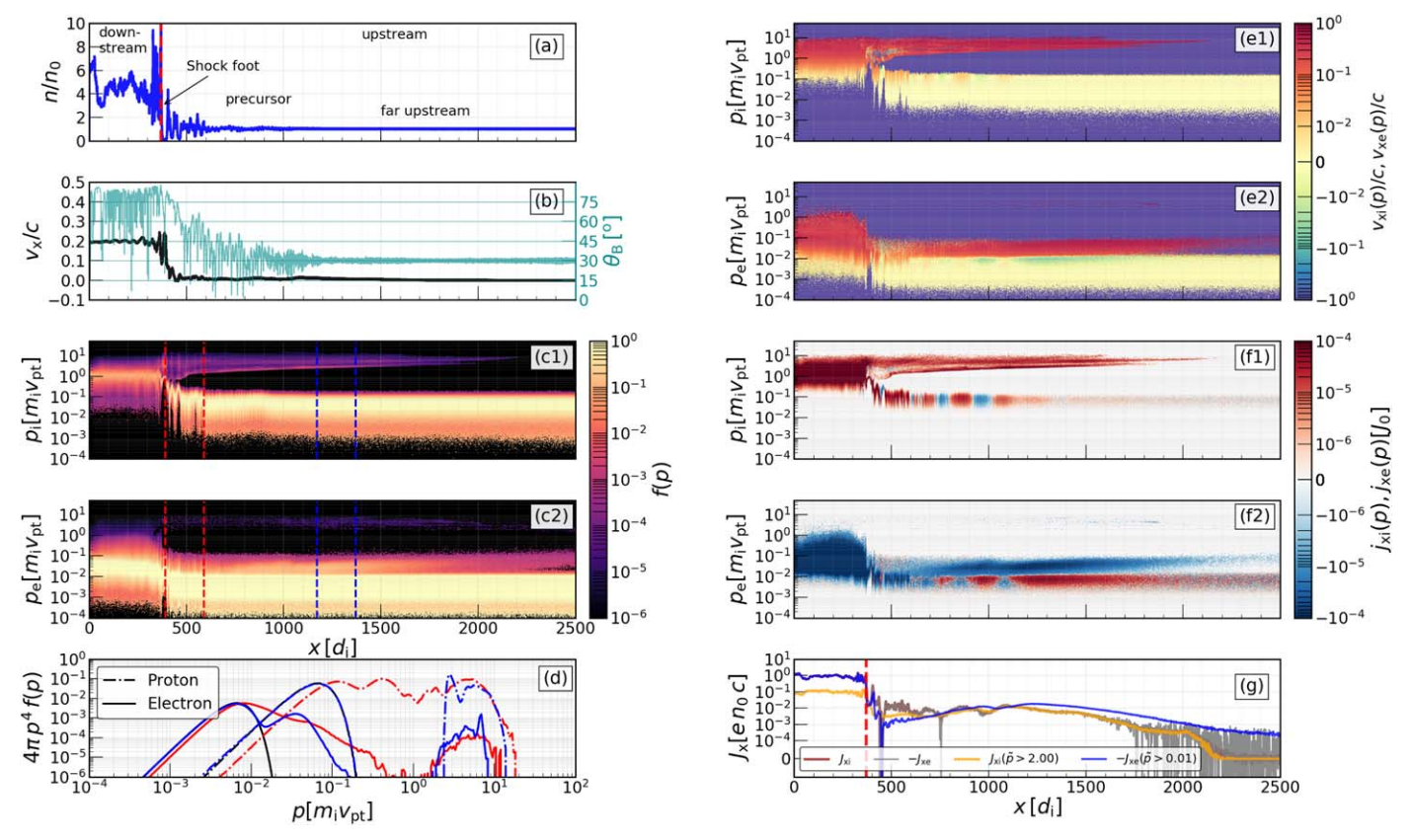


Figure 1. Profiles of different physical quantities at $t=85~\omega_{\rm ci}^{-1}$ for our benchmark shock simulation with $v_{\rm pt}/c=0.2$, $\mathcal{M}_{\rm A}=20$, $\mathcal{M}_{\rm S}=40$, $\theta_{\rm Bn}=30^{\circ}$, and $m_{\rm R}=100$. Panels (a) and (b) display density and total (thermal + NT) x-velocity. Panels (c1) and (c2) show the x-p phase space for protons and electrons, and panel (d) shows their momentum spectra in the two upstream regions marked in panels (c1) and (c2). The x-velocity (Equation (1)) and current density (Equation (2)) for protons and electrons as a function of momentum p are displayed in panels (e1), (e2), (f1), and (f2), respectively. Panel (g) shows total and partial currents, as in the legend; note that, although the net currents are balanced, NT protons $(p/m_i v_{\rm pt} \gtrsim 2$, orange) and ST+NT electrons $(p/m_i v_{\rm pt} \gtrsim 0.01$, blue) constitute currents that are sometimes larger or smaller than the total current in the respective species.

The discussion above shows that the particle distributions upstream of quasi-parallel shocks readjust automatically in response to the currents launched by the shock. In Sections 4–6, we quantify how and where the ST electrons are produced, and the ensuing electron heating.

4. Production Sites and Mechanisms

In this section, we study the microphysics of generation of ST electrons that provide the return current. We focus on two distinct regions: far upstream and close to the shock, as illustrated in the following.

4.1. Far Upstream

Let us consider a region far from the shock and investigate the response of background plasma to NT protons. To do this, we track $(4+4)\times 10^4$ thermal protons and electrons starting in the pristine upstream medium (position $x_{\rm ini}$); their evolution at $t=78.7~\omega_{\rm ci}^{-1}$, $121.9~\omega_{\rm ci}^{-1}$, and $140.9~\omega_{\rm ci}^{-1}$ is shown in three columns of Figure 2.

Figures 2(a1)–(a3) show the proton x–p phase space. The x– v_x phase space of the tracked protons and electrons are shown in Figures 2(b1)–(b3) and (c1)–(c3), along with the profile of B_z , with particles color-coded according to their momentum (rightmost color bar). Figures 2(d1)–(d3) show the spectrum of the tracked protons and electrons, which are initially thermal as seen by comparing the blue and red curves with black (Maxwellian) curves. Figures 2(e1)–(e3) show the

Fourier analysis of E_x in the gray region of Figures 2(b1)–(b3) and (c1)–(c3).

When the NT protons reach $x_{\rm ini}$ (the middle column), a distinct electrostatic (ES) mode appears (Figure 2(e2)), which is due to interactions between the current beam and thermal plasma. The wavenumber of the mode is found to be (see Appendix)

$$k = \frac{\omega_{\text{pe}}}{v_{\text{ib}}} = \frac{\sqrt{m_{\text{R}}}}{v_{\text{ib}}/c} d_i^{-1},\tag{3}$$

where $v_{\rm ib} \gtrsim 2 \, v_{\rm pt}$ is the drift velocity of the current-driving protons. The middle column also shows that the tracked protons remain thermal, while several electrons achieve ST momenta and start moving toward upstream infinity. The energization of these electrons is evident in Figure 2(d3), corresponding to $t=140.9~\omega_{\rm ci}^{-1}$, where the electron distribution exhibits an ST hump similar to Figure 1(d). Note that the ES mode has also disappeared, which means that the proton beam has eventually transferred a fraction of its energy to the background electrons.

As the shock moves, the NT beam becomes less anisotropic and the current in the region $x_{\rm ini}$ increases, which can drive EM instabilities; the whole background will eventually thermalize to a higher temperature. However, the above scenario may still be valid in the far upstream where the charged beam penetrates the fresh plasma, as long as the current in the beam is not negligible. Thus, the result provides clear evidence that: (1) the

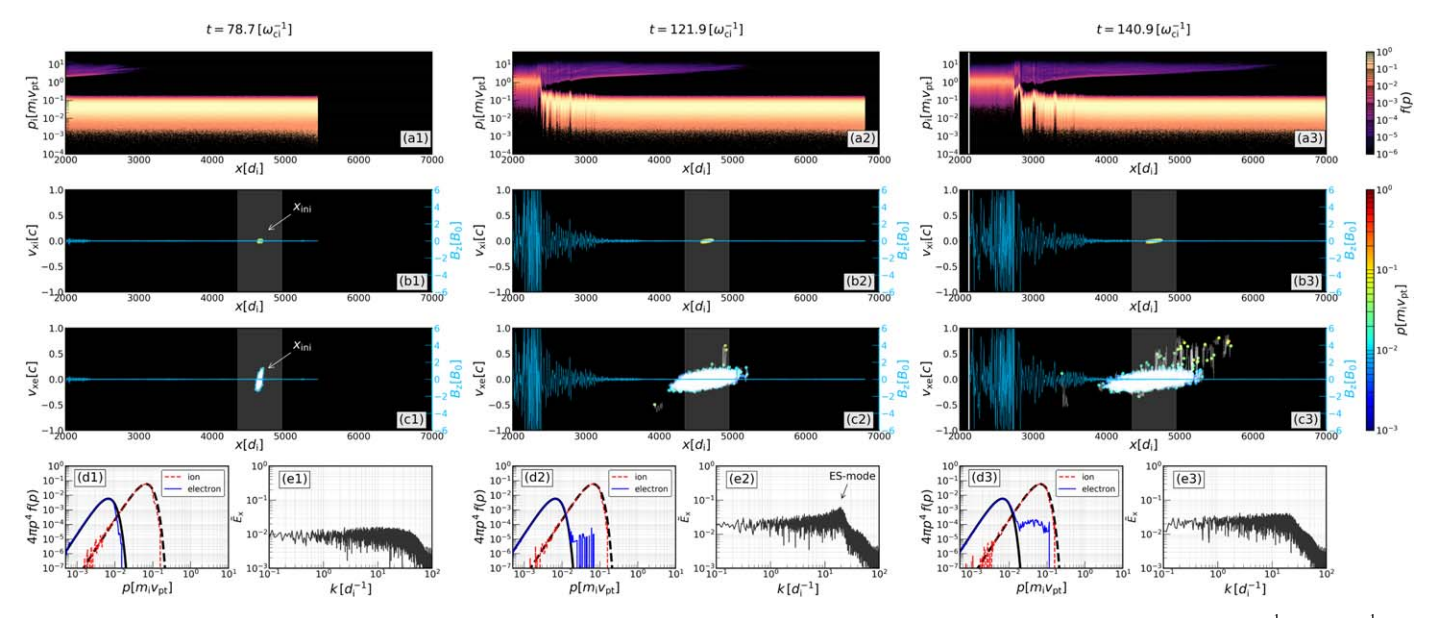


Figure 2. Development of the ST electrons in the far upstream of a quasi-parallel shock. Columns from left to right correspond to $t = 78.7 \, \omega_{\rm ci}^{-1}$, $121.9 \, \omega_{\rm ci}^{-1}$, and $140.9 \, \omega_{\rm ci}^{-1}$. Panels (a1)–(a3) show the proton x–p phase space, while panels (b1)–(b3) and (c1)–(c3) show the x– ν_x phase space of tracer protons and electrons; the blue curves indicate B_z . Note that the horizontal axes in these panels represent the distance in the upstream rest frame. Panels (d1)–(d3) show the momentum distribution of the tracked electrons/protons, and panels (e1)–(e3) display the mode analysis of $|E_x|$ in the highlighted region of panels (b1)–(b3) or (c1)–(c3). When NT particles enter the region (middle column), protons remain thermal; however, electrons develop ST, back-streaming population well before they reach the shock.

ST electrons that contribute to the return current can be produced locally in the upstream, and (2) a population of back-streaming electrons in the upstream is not necessarily a signature of injection into DSA.

4.2. Immediately Upstream of the Shock

The characterization of the return current very close to the shock is challenging, since different instabilities operate simultaneously. On top of the streaming instability driven by DSA protons, the shock foot (i.e., the region immediately upstream of the shock) also experiences the current of specularly reflected thermal protons, which drives the reformation of any supercritical shock (e.g., Treumann 2009) on a cyclotron timescale (e.g., Thomas et al. 1990; Lee et al. 2004; Caprioli et al. 2015). These reflected protons can create a scenario similar to the far upstream (Section 4.1), as we illustrate below.

Figures 3(a) and (b) show the evolution of the $x-v_x$ phase space for protons and electrons between $t = 280.3 \,\omega_{\rm ci}^{-1}$ and $282.7 \ \omega_{ci}^{-1}$. Times are chosen in order to illustrate one cycle of shock reformation. Initially, we see a beam of specularly reflected protons with velocity $v_{\rm ib} \approx 0.4c~(\equiv 2v_{\rm pt})$; the left edge of the proton beam represents the old location of the shock, and the right one marks the location where the new shock barrier will reform. At $t = 280.3 \ \omega_{ci}^{-1}$, the electron phase space shows two distinct populations: one close to the old shock barrier and another in the middle of the proton beam, indicated by the arrows. The former population corresponds to shock-reflected electrons, while the latter arises directly because of the proton beam and not because of reflection from the shock; the electrons in this ST population have a v_x velocity that exceeds the shock speed, which means that they stream away upstream. Both features fade away when the proton beam disappears (i.e., when the new barrier is formed), as shown in the snapshot at 282.7 ω_{ci}^{-1} . Thus, the shock reformation periodically produces a population of back-streaming electrons.

To understand how the back-streaming electrons formed, we plot the profiles of $E_{x,y}$ and B_z in Figure 4(a) and their mode diagnostics in Figures 4(b1) and (b2), for the same two epochs considered in Figure 3. First, we notice that, in the downstream, $E_{\rm v} \approx v_{\rm pt} B_{\rm z}/c$ (the red curve appearing as purple due to the mixing with blue), as expected for the transverse motional electric field (y-z) produced due to the bulk speed of downstream plasma in the upstream frame. The parallel component E_x cannot be totally motional, and in fact it develops due to the pressure anisotropy in different populations. Importantly, the Fourier analysis shows that a distinct ES mode appears around $k \approx 20~d_i^{-1}$ at 280.3 $\omega_{\rm ci}^{-1}$, i.e., when the proton current is strong (Figure 3). The wavenumber of this mode is consistent with Equation (3), which indicates that the nature of the instability is similar to the two-stream instability or the Buneman instability (Hoshino & Shimada 2002; Bret & Dieckmann 2010; Muschietti & Lembège 2017). This instability is modulated with the quasi-periodic proton reflection and produces a parallel E_x that can scatter and energize electrons.

5. The Fate of Return-current Electrons

In the previous section, we have discussed how ST electrons are produced locally at the shock and far upstream in response to the proton-driven current. In a global shock simulation, at any point in the upstream, one in principle has the contribution from ST electrons produced in the shock foot, as well as the ones locally produced by the streaming protons and those reflected from the shock. In order to disentangle such contributions and to assess the long-term evolution of such ST electrons, we perform controlled simulations with different proton beams without including the shock. In the end, we show that, depending on the distribution of the proton beam and the time for which electrons are exposed to it, their evolution can be different.

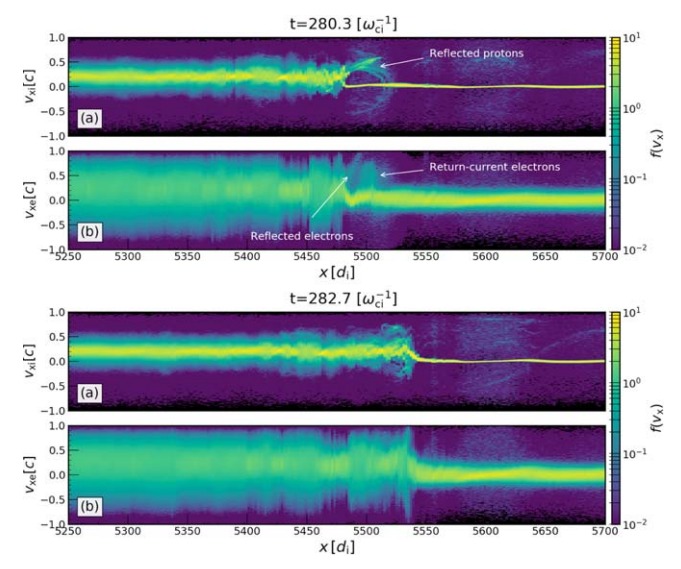


Figure 3. $x-\nu_x$ phase-space distribution of protons (panel (a)) and electrons (panel (b)) at $t=280.3~\omega_{\rm ci}^{-1}$ and $282.7~\omega_{\rm ci}^{-1}$ (top and bottom panels, respectively). The arrows in the top panels indicate the specularly reflected protons and the two distinct populations of high- ν_x electrons: those reflected at the shock ramp and those produced by the proton current. Both populations vanish in the bottom panels.

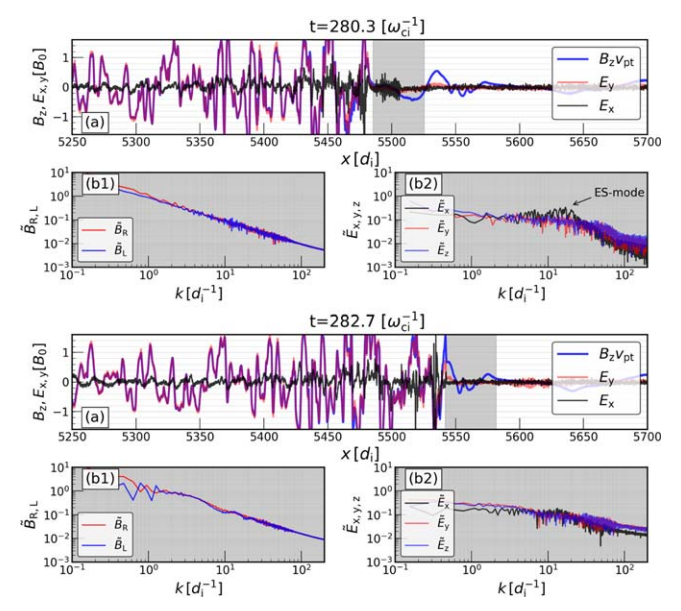


Figure 4. Diagnostics of the EM profiles at two different times as shown in Figure 3. The panel (a) shows the profiles of E_x , E_y , and B_z . The foot of the shock is highlighted by the gray region. The panels (b1) show the Fourier analysis of the right and left circular modes $(\tilde{B}_{R,L} = \tilde{B}_y \pm j\tilde{B}_z)$, and panel (b2) represents the Fourier analysis of E_x , E_y , and E_z in the gray region. When the shock is reforming (at $t = 280.3 \,\omega_{ci}^{-1}$), the appearance of an ES mode is evident.

5.1. Setup of Controlled Simulations

We set up the thermal plasma parameters similar to our shock run, but with periodic boundary conditions in all directions. The time stepping Δt , the number of cells per $d_{\rm e}$, the magnetization of the plasma, and the current filtering are chosen to be identical to those in our shock setup (see Section 2). The number of particles per cell per species is set to 100, and the size of the 1D computational domain along x is fixed to $300 d_i$, where the fiducial $m_{\rm R} = 100$. In

Table 1

The Beam Parameters for Our Benchmark Controlled Simulations,
Representing Three Distinct Regions in the Upstream, as Shown in Figure 1(a)

Region	Beam Type	$n_{\rm ib}/n_{\rm 0}$	$v_{\rm ib}/c$	$p_{ib}/m_i c$
1. Far upstream	dilute cold	0.005	0.4	0.4
2. Precursor	dilute hot	0.005	0.3	0.5
3. Shock foot	dense cold	0.1	0.4	0.4

Note. For the background plasma: $v_{\rm A}/c=1.33\times 10^{-2}, v_{\rm th,i}/c=6.67\times 10^{-3},$ and $m_{\rm R}=100$ (corresponding to a Debye length =0.067 $d_{\rm e}$). The drift velocity and the average momentum along the x-direction are provided in the background plasma rest frame (obtained using Equations (12) and (13) in Gupta et al. 2021).

addition to background electrons and protons (initialized to a Maxwell–Boltzmann distribution), we introduce a third species that represents the beam protons; the beam-to-background proton density ratio, $n_{\rm ib}/n_0$, is implemented by varying the weight of the species, which ensures charge neutrality of the whole system as well as zero electric field at the beginning (see also Riquelme & Spitkovsky 2009; Gupta et al. 2021). In the benchmark run, we apply a boost speed of $v_{\rm bst} = 0.4c \ (\equiv 2 \ v_{\rm pt})$ to the current-driving protons, without imposing any bulk speed on the background plasma to compensate for such a current. In this way, we can observe the development of the return current from scratch. Nevertheless, we observed that the outcomes remained unaffected, even when the return current was introduced at the initial time (t = 0). The one remaining parameter is the velocity distribution of the beam protons that determines the drift speed v_{ib} relative to the background plasma frame in this setup (see Equation (12) in Gupta et al. 2021); this parameter is chosen as follows.

We consider two cases: (1) a cold beam with the speed of particles in the beam rest-frame $u_{\rm iso} \simeq 0$ (or $u_{\rm iso} \ll v_{\rm ib}$), and (2) a hot beam with $u_{\rm iso} \gtrsim v_{\rm ib}$. The former case is a representative of the shock foot (specularly reflected protons, e.g., Figure 3) or far-upstream region (particles escaping upstream infinity, e.g., Figure 2), whereas the latter case stands for the shock precursor, where the beam is diffusing. The run parameters of these simulations are listed in Table 1. While such numbers may vary depending on the shock speed or the momentum/energy of the NT particles, the beam type and consequently its influence on the plasma are expected to remain consistent with the findings that we explore in the following sections. Note that, although we discuss dilute/dense cold/hot cases separately, in a realistic scenario, the plasma experiences both as the background thermal populations move close to the shock.

5.2. Results

5.2.1. Cold Beams

We consider two limiting regimes: a dilute beam $(n_{\rm ib}/n_0 \lesssim 0.01, {\rm region~1~in~Table~1})$ and a dense beam $(n_{\rm ib}/n_0 \sim 0.1, {\rm region~3})$. The dilute beam is representative of the beam of energetic protons streaming away far upstream, while the dense beam in the shock foot is produced by the specular reflection at the shock.

We start with the case of the dilute beam with $n_{\rm ib}/n_0=0.005$. Figures 5(a1)–(b3) show the x–p phase-space distribution of the current density j_x at t=0, 1, and 150 $\omega_{\rm ci}^{-1}$; the gray lines indicate the profile of B_z (values on the right axes). At t=0, i.e., Figures 5(a1) and (b1) show that the current

density is nonzero only for the proton beam ($j_x \simeq 0.15 e n_0 v_A$), while the background plasma has random fluctuations that average to zero. Figures 5(c) and (d) show the spectra and the beam-induced modes, respectively, as discussed below.

At $t=1~\omega_{\rm ci}^{-1}$, we observe the appearance of ST electrons and of the ES mode, as shown in Figures 5(b2), (c), and (d), similar to what happens far upstream (Figure 2). Moreover, for these parameters, the ratio of the beam momentum ($P_{\rm ib}=n_{\rm ib}p_{\rm ib}$) to the magnetic pressure $P_{\rm ib}/P_{\rm B0}\approx 10$ satisfies the nonresonant instability (e.g., Bell 2004; Gupta et al. 2021, especially Equation (9)), i.e., $\delta B/B_0 \gtrsim 1$ can be expected (Gupta et al. 2022). However, since the growth rate of the fastest-growing mode is $\gamma_{\rm fast}=0.5(n_{\rm ib}/n_0)(\nu_{\rm bi}/\nu_{\rm A})\omega_{\rm ci}=0.08~\omega_{\rm ci}$, it takes a few ion cyclotron times to grow B_z appreciably.

At a later time, $t=150~\omega_{\rm ci}^{-1}$, we see that the overall electron

At a later time, $t=150~\omega_{\rm ci}^{-1}$, we see that the overall electron distribution has shifted to a high-temperature thermal-like distribution and the ES mode has faded away (Figures 5(c) and (d)). Thus, the ST electrons that we have observed in this dilute cold beam simulation as well as in the far upstream can be considered the early phases of electron energization, which is initially driven by ES instability and later by the EM turbulence of the streaming instabilities. Eventually, the current is disrupted and the whole background moves along the direction of the beam, due to the linear momentum conservation. Finally, we note that, at saturation, $\delta B/B_0 \approx 1$; this is consistent with the fact that the Bell instability saturates at $B_z/B_0 \approx \sqrt{P_{\rm ib}/P_{\rm B0}} \sim 1$, where $P_{\rm ib}/P_{\rm B0} \simeq 10$ (e.g., Gupta et al. 2021, 2022; Zacharegkas et al. 2022).

When the beam is dense (representing region 3 in Table 1), we find a similar evolution, with the exceptions that: (1) the beam current $j_x \simeq 3 \ e \ n_0 \ v_A$ is too strong to drive nonresonant instability, since it makes $\gamma_{\rm fast}/\omega_{\rm ci} \equiv j_x/(2 \ n_0 \ e \ v_A) > 1$, which does not favor the traditional nonresonant instability (e.g., Zweibel & Everett 2010; E. Lichko et al. 2024, in preparation), and (2) the thermalization is achieved within $\lesssim 2 \ \omega_{\rm ci}^{-1}$ (i.e., much earlier than that found in the dilute beam case), upon which we will elaborate in Section 6.

5.2.2. Hot Beams

In the shock precursor, the particles are diffusing and thus more isotropic, i.e., the beam cannot be considered cold. To study the response of background electrons in this region, we use a hot beam $(u_{\rm iso} \gtrsim v_{\rm ib})$; see region 2 in Table 1). In this case, instead of a distinct E_x mode, broadband fluctuations arise, similar to those in Figure 4(b2) at $t=282.7~\omega_{\rm ci}^{-1}$, i.e., when the current is mostly driven by diffusing particles. In this scenario, the response of the background plasma is incoherent on spatial scales of the E_x modes, which are approximately on the order of $2\pi(v_{\rm ib}/c)d_{\rm e}$ (Equation (3)). As in the cold case, the later evolution is characterized by the growth of nonresonant modes and acceleration of the background plasma in the direction of the beam.

To summarize, our controlled simulations of different types of beams, corresponding to three distinct regions of the upstream (Table 1), show that current compensation invariably leads to the production of ST electrons, similar to those appearing in the global shock simulation (Section 4). While back-streaming ST electrons are indeed a transient phenomenon, they are always present far upstream, and may be mistakenly taken for accelerated particles. We have also investigated the long-term evolution of the ST electrons and found that ST electrons are thermalized, which contributes to

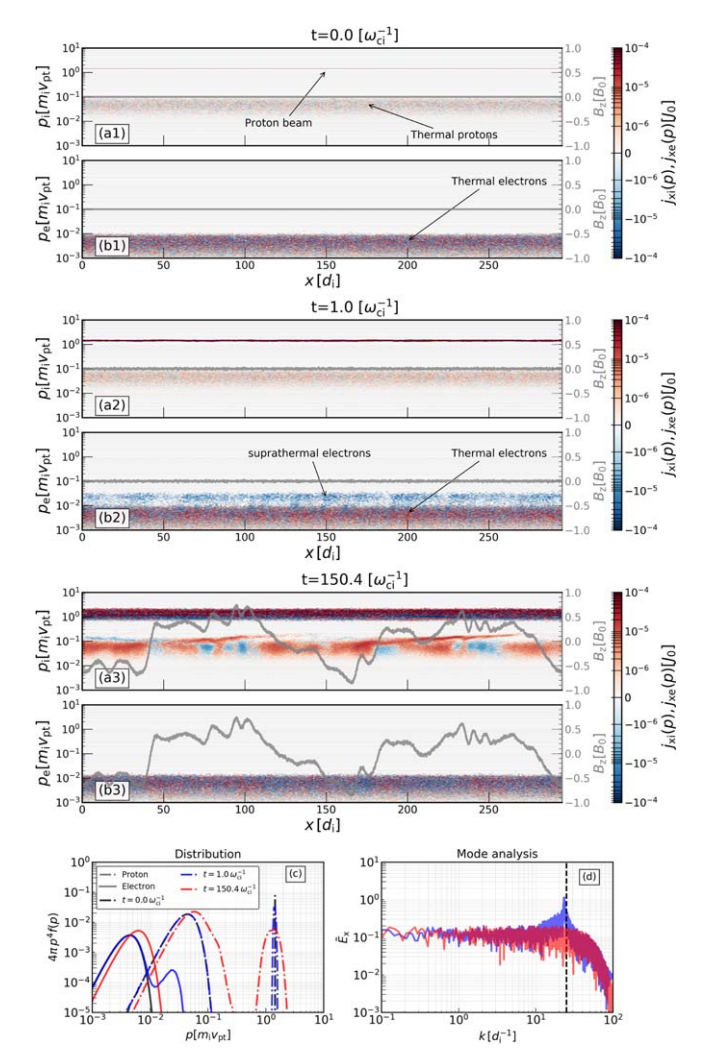


Figure 5. A controlled simulation showing the development of return-current electrons due to a cold proton beam (region 1 in Table 1). Panels (a1)–(a3) and (b1)–(b3) represent the x–p phase space of j_x for protons and electrons, along with profiles of the magnetic field (gray curves and right axes) at t=0,1, and $150~\omega_{\rm ci}^{-1}$. The spectra of protons and electrons and the Fourier analysis of E_x corresponding to those times are displayed using black, blue, and red colors in panels (c) and (d), respectively. The proton spectra also contain the beam distribution ($p \gtrsim m_i v_{\rm pt}$, where $v_{\rm pt} = v_{\rm ib}/2$), which is renormalized to keep the beam spectra within the chosen y-range. In panel (d), the vertical line shows the predicted ES mode for the parameters used in this setup (Equation (3)). Development of ST electrons is evident at $t=1\omega_{\rm ci}^{-1}$. In the late times, the ES mode and the ST hump in the electron distribution disappear and the whole background plasma attains a nonzero bulk motion along the direction of the beam.

overall heating, as shown in Figure 5(c). Since the current is relatively small at large distances, we do not expect a substantial level of heating when averaging over all electrons in the far-upstream region, and in general not beyond the heating that the Bell instability provides (e.g., Caprioli & Spitkovsky 2014a; Gupta et al. 2022). However, we will show that this changes closer to the shock under the action of the dense beam of specularly reflected protons in the shock foot (Figure 3).

6. Electron Heating in the Shock Foot

Before encountering the shock, the upstream plasma has to experience the dense $(n_{\rm ib}/n_0 \sim 0.1)$ reflected proton beam in

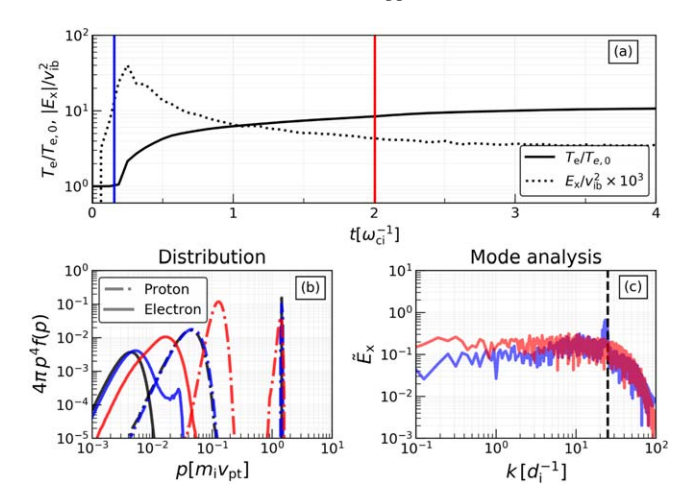


Figure 6. Response of background plasma in the case of cold dense beam (region 3 in Table 1). Panel (a) displays the time evolution of E_x and T_e . Panels (b) and (c) represent the momentum distribution of electrons/protons and the Fourier analysis of E_x at two epochs marked in panel (a). The vertical dashed line in the panel (c) represents the expected wave mode (k) from Equation (3). Note the net heating is more intense than that found for the far-upstream dilute beam case (Figure 5(c)).

the foot. Such an interaction is important for electron heating and potentially injection into DSA. To quantify electron heating in the shock foot, we have performed a set of controlled simulations for a wide range of beam and background plasma parameters. For each simulation, we calculate the effective electron temperature tensor,

$$k_{\rm B}T_{\rm rs} \equiv \frac{1}{N_{\rm e}} \int \gamma \ u_r(p') u_{\rm s}(p') f(p') d^3 p', \tag{4}$$

where r, $s \in x$, y, z, N_e is the total number of electrons in the computational domain, and u_r is the velocity in the r-direction, which is obtained by transforming it to the comoving plasma frame. We call this an effective temperature because the electron distribution is not Maxwellian, and its shape evolves with time. To find a correlation with the ES mode, we also estimate the volume averaged absolute value of E_r .

Figure 6 presents the results of our benchmark dense cold beam simulation (region 3 in Table 1). Panel 6(a) shows that there is an initial stage ($\sim 0.1~\omega_{\rm ci}^{-1}$) when the effective temperature $T_{\rm rr}$ (hereafter, $T_{\rm e}$) does not change much, whereas E_x raises rapidly. After E_x reaches a peak ($E_x/v_{\rm pt}^2 \sim 0.03~(B_0/c^2)$), it damps and $T_{\rm e}$ increases. When $t\gtrsim 1~\omega_{\rm ci}^{-1}$, $T_{\rm e}$ tends to $\sim 9T_{\rm e,0}$ ($T_{\rm e,0}$ being the initial temperature). These initial and final stages are displayed in Figures 6(b) and (c), which show that (1) the ST hump evolves to a thermal-like distribution and (2) the E_x mode disappears, similar to the case of a dilute cold beam case (Figure 5).

The dependence of electron heating from the shock/simulation parameters is further detailed in Figures 7 and 8. In both figures, the red star represents our benchmark dense cold beam simulation (discussed above), with other runs differing from the benchmark in one of these parameters, as listed in the legend. We consider the evolution of the electron temperature from t=0 to t=2 $\omega_{\rm ci}^{-1}$, physically corresponding to the time that it takes for the shock to overtake the shock foot, and compare the final electron thermal speed with the initial proton beam velocity; note that T_e is already very close to saturation, as shown in Figure 6(a).

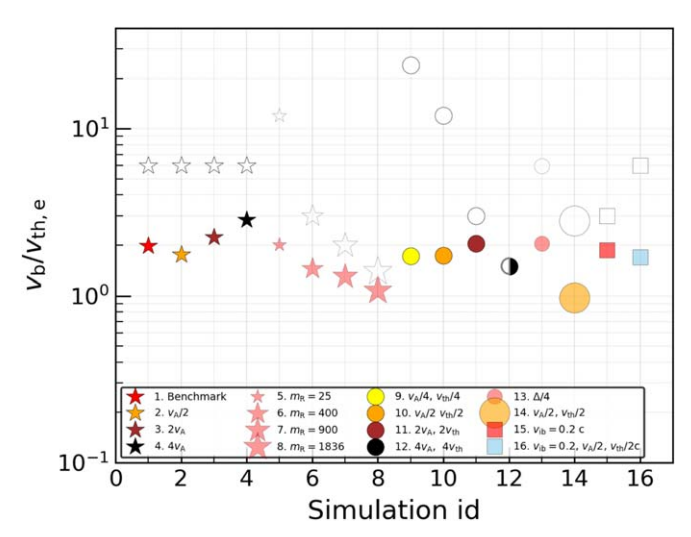


Figure 7. Level of electron heating for different parameters (mass ratio m_R , magnetization v_A , thermal speed v_{th} , beam velocity v_{ib} , and the grid spacing Δ). The vertical axis displays the ratio of beam velocity (v_{ib}) to the effective thermal speed of electrons $v_{th,e} = (k_B T_e/m_e)^{1/2}$ obtained from a set of controlled simulations by varying one parameter at a time relative to the benchmark run (region 3 in Table 1), where the empty and filled symbols represent t=0 and the filled symbols $t=2\,\omega_{ci}^{-1}$, respectively. The horizontal axis denotes the IDs of different simulations (identical to the legend number).

For the benchmark run, Figure 7 shows that the initial ratio $v_{\rm ib}/v_{\rm th,e} \simeq 6$ drops to ≈ 2 (white and red stars, respectively), corresponding to an increase in electron temperature of a factor of 9. Very interestingly, changing the beam/background parameters does not change the fact that, at saturation, electrons are heated up until their thermal speed becomes on the order of the proton beam velocity, as shown in Figure 7. This universality can be explained by considering the beam-induced ES mode, which is the main driver of electron heating at the shock foot (see, e.g., Figure 5).

Figure 8 shows the peak amplitude of E_x for the simulations in Figure 7. First, we observe a positive correlation between $T_{\rm e}$ and E_x , as expected from the above discussion of the benchmark run (Figure 6). Second, we see that $E_x \propto v_{\rm ib}^2$ (light blue square versus the benchmark run) for a fixed beam density, which suggests that the strength of the ES mode depends on the kinetic energy density of the beam. Third, E_x decreases with the mass ratio (red stars with increasing size), yet yielding the same final $v_{\rm ib}/v_{\rm th,e}$. This trend can be accounted for by noticing that a larger $m_{\rm R}$ reduces the difference between $v_{\text{th,e}}$ and v_{ib} that enters the dispersion relations (see Appendix). This suggests that, for realistic values of $m_{\rm R}$, the amplitude of the current-induced E_x mode may decrease, but without changing the final $v_{ib}/v_{th,e}$ ratio. We also verified that the final temperature is insensitive to the grid resolution (red star versus red circle).

Since in general $v_{ib} \sim v_{sh}$, in the absence of upstream heating, the electron sonic Mach number $\mathcal{M}_{s,e,0} \equiv v_{sh}/v_{th,e}$ could span orders of magnitude, from $\mathcal{M}_{s,e} \sim 1$ in heliospheric and intracluster shocks to $\mathcal{M}_{s,e} \gg 1$ shocks in the interstellar medium. However, we have shown that, when the proton beam velocity is larger than the thermal speed of background electrons, the shock foot is prone to an ES instability driven by an initial current imbalance, which grows on a timescale $\ll \omega_{ci}^{-1}$ (see, e.g., the Appendix). The energy associated with the fluctuating E_x is quickly transferred to the background, and in particular to the electrons, which heat up to $v_{th,e} \approx v_{ib}$. As a

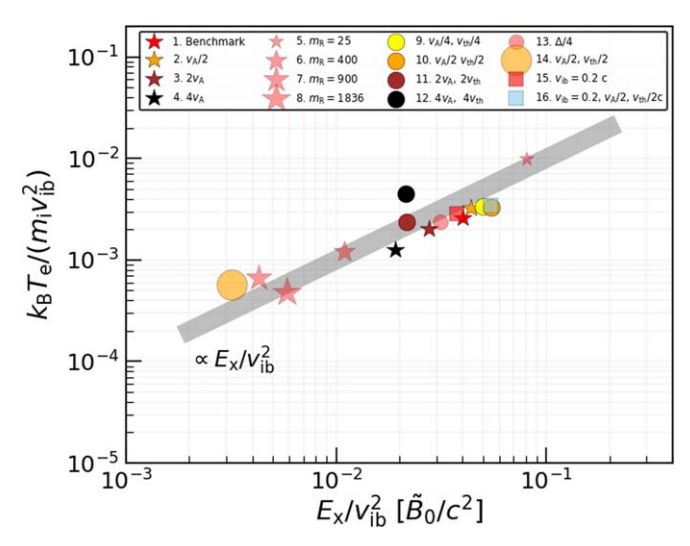


Figure 8. Correlation between the effective temperature of electrons at $t = 2 \omega_{\rm ci}^{-1}$ and the peak amplitude of the beam-induced ES mode $E_x/v_{\rm ib}^2$, showing $T_{\rm e} \propto E_x$ (label IDs are identical to Figure 7).

result, the effective sonic Mach number for electrons in the shock foot becomes $M_{\rm s,e} \equiv v_{\rm ib}/v_{\rm th,e} \approx 1-3$ (see Figure 7), independent of the initial sonic Mach number. While it may be a semantic question whether heating in the foot can be considered to occur *upstream* of the shock versus at the shock, this finding has implications not only for the temperature that electrons achieve behind the shock, but also for the injection of electrons into DSA. In fact, a larger thermal speed facilitates magnetic mirroring (e.g., Guo et al. 2014a) and hence electron reflection and acceleration (S. Gupta et al. 2024, in preparation).

7. Return Currents in Quasi-perpendicular Shocks

So far, we have discussed return currents in the context of quasi-parallel shocks, but it is worth discussing what happens when the shock is quasi-perpendicular, too. It is already known that oblique shocks reflect more electrons than protons (Guo et al. 2014a, 2014b; Xu et al. 2020; Bohdan et al. 2022; Morris et al. 2022), which implies that the unbalanced current in the upstream should be carried by back-streaming electrons and that the return current must be positive.

We perform simulations of quasi-perpendicular shocks with $\theta_{\rm Bn}=63^{\circ}$, keeping all the other parameters identical to our benchmark shock run ($v_{\rm pt}=0.2~c$, $\mathcal{M}_{\rm A}=20$, $\mathcal{M}_{\rm s}=40$, and $m_{\rm R}=100$). Figures 9(a) and (b) show the phase-space distribution of current density (j_x) for protons and electrons at $t=45~\omega_{\rm ci}^{-1}$, respectively. Figure 9(a) shows that the proton population upstream is completely thermal, while the electron population in Figure 9(b) displays three district features, as labeled. In this scenario, the unbalanced current is induced by the reflected electrons, which also develop the ES mode (Bohdan et al. 2022). The return current is carried by background electrons, which move toward the shock, while staying close to thermal. In fact, the current in back-streaming electrons does not carry much momentum/energy, thereby not leading to any appreciable heating.

Our study demonstrates that the distributions of upstream particles readjust automatically to neutralize the total currents in the plasma, regardless of the initial inclination of the magnetic field relative to the shock normal. These processes

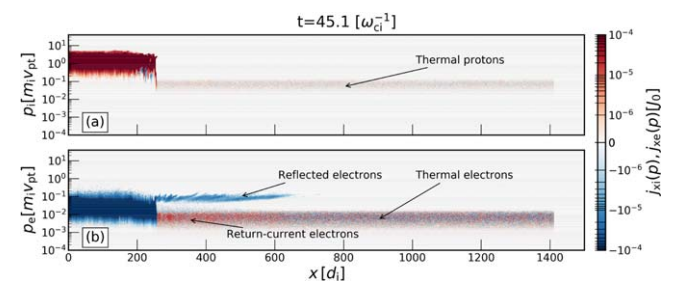


Figure 9. Current diagnostics for a quasi-perpendicular ($\theta_{Bn}=63^{\circ}$) shock. The panels (a) and (b) stand for protons and electrons, respectively. The distinct populations upstream are marked by the arrows (also compare with Figure 1(f1) and (f2)).

primarily affect electrons: if the driving current carries strong enough momentum, then electrons may become hot/suprathermal and either move toward the shock or upstream, depending on the direction of the dominant current in the driving beam. While throughout this work we take $v_{\rm pt}/c = 0.2$, to discuss the production mechanism and the evolution of suprathermal electrons, we find that the results persist even when considering smaller values of $v_{\rm pt}/c$, in particular when the upstream electrons are initially cold and moderately less magnetized, as typically found in a high Mach number shock ($\mathcal{M}_{s,e} > 1$ and $\mathcal{M}_{\rm A} \gtrsim 10$). We expect that the general conclusions should qualitatively hold for $v_{\rm pt}/c > 0.2$. An in-depth examination of trans-relativistic shocks is beyond the scope of present work, since multidimensional effects are crucial for the self-generation of the NT current beam upstream of such shocks (Crumley et al. 2019).

8. Summary

In this work, we have used particle-in-cell simulations to study the balance of electric currents upstream of collisionless shocks and their impact on electron distribution. We have developed a diagnostic to identify the return-current populations and confirmed our results by designing a controlled test problem. Our main findings are summarized below:

- 1. Whenever an unbalanced current is produced in the plasma due to particles reflected from the shock, the system pulls electrons out of the thermal background via an electrostatic process akin to the two-stream instability (Figure 5).
- 2. Depending on the direction of the unbalanced current in the upstream frame, compensating electrons can either move toward the upstream infinity or toward the shock (back-streaming or forward-streaming electrons, respectively). The former scenario is typical of quasi-parallel shocks, where the current is carried by nonthermal (NT) ions (Figure 1). The latter scenario occurs for quasi-perpendicular shocks, where the currents are typically made of electrons (Figure 9).
- 3. In the shock upstream, the driving current-induced electrostatic mode transfers its energy to background thermal electrons and generates a population of suprathermal (ST) electrons. Such ST electrons carry the return current and can be found anywhere from the far upstream to the shock foot (Figures 2 and 3). Given the nonthermal nature of these electrons, they may be easily confused with electrons that are experiencing DSA. We show that back-streaming ST electrons can be produced locally in

the upstream well before they interact with the shock (Figure 2).

- 4. During the initial stages of interaction between the current beam and the thermal plasma (either far upstream or during the quasi-periodic shock reformation), the distribution of the return current electrons may appear as an ST hump attached to the thermal distribution. Then, while being advected toward the shock, these electrons are progressively thermalized (Figure 6).
- 5. In the shock foot, there periodically appears a strong unbalanced proton current due to the shock reformation (Figure 3). A crucial byproduct of such a current imbalance in the shock foot is the strong heating of thermal electrons. This effect is noticeable mainly when the thermal speed of background electrons is smaller than the velocity of the current-producing beam (Section 6). By performing a set of controlled simulations, we find that the final thermal speed of the electrons generally becomes comparable to the velocity of the proton beam (Figure 7). This is a nontrivial finding which suggests that the effective electron sonic Mach number close to the shock should generally be ≤1–3. This energization can potentially simplify the process of reflecting and injecting electrons into DSA.

To conclude, we have detailed the production mechanism and the properties of the electrons that make up return currents in collisionless shocks. How these results may help fostering our understanding of injection and DSA of electrons will be discussed in forthcoming papers.

Acknowledgments

S.G. thanks Emily Lichko and Vladimir Zekovic for insightful discussions. We thank the referee for providing valuable constructive suggestions. We acknowledge the computational resources provided by the University of Chicago Research Computing Center and ACCESS (TG-AST180008). D.C. was partially supported by NASA through grants 80NSSC20K1273 and 80NSSC18K1218 and NSF through grants AST-1909778, PHY-2010240, and AST-2009326. A.S. acknowledges the support of grants from NSF (PHY-2206607) and the Simons Foundation (MP-SCMPS-00001470).

Appendix

A Cold Current Beam in a Warm Electron-Proton Plasma

To understand the role of electron temperature in a beamplasma system, we investigate its dispersion equation. Considering that the system consists of three species—respectively, background protons, background electrons, and a cold beam made of either protons or electrons—we obtain a dispersion equation for the modes parallel to the beam direction:

$$\frac{\omega_{\rm pi}^2}{\omega^2} + \frac{\omega_{\rm pe}^2}{\omega^2 - a_{\rm th,e}^2 k^2} + \frac{n_{\rm b}/n_0 \omega_{\rm b}^2/\gamma_{\rm b}^3}{(\omega - v_{\rm b}k)^2} \simeq 1.$$
 (A1)

Here, we have assumed that the electrons have non-negligible sound speed $a_{\rm th,e} (\equiv \sqrt{5/3} \, v_{\rm th,e})$, the magnetic field is negligible (weakly magnetized plasma), the beam density $n_{\rm b}$, $\omega_{\rm b} = \sqrt{4\pi n_{\rm b} e^2/m_{\rm b}}$, and the Lorentz factor $\gamma_{\rm b}$. $m_{\rm b}$ is the mass of individual particles in the beam, either m_i or $m_{\rm e}$, depending on the current dominant species. A similar equation can be

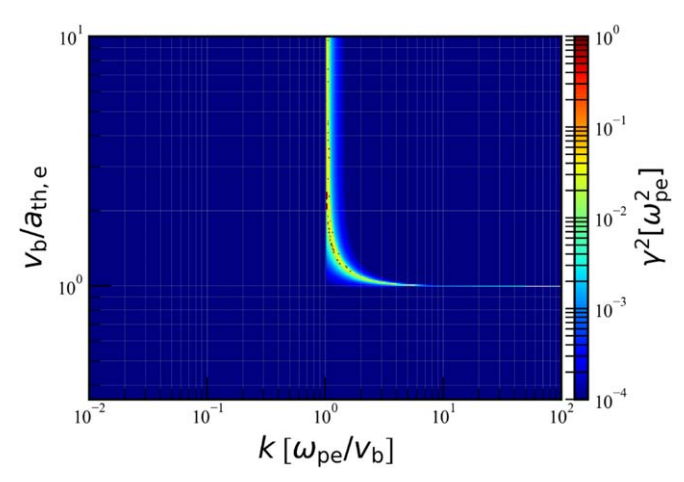


Figure 10. Solution of the dispersion Equation (A1) as function of k for different values of $v_{\rm b}/a_{\rm th,e}$ and a fixed $n_{\rm b}/n_{\rm 0}$.

found in Bret & Dieckmann (2010), where the system consists of a beam of relativistic electrons and a cold background plasma.

Substituting ω by $\omega_{\rm R}+j\,\gamma$ (where $\omega_{\rm R}$ and γ represent the real and growing/damping terms, and $j=\sqrt{-1}$), Equation (A1) can be solved numerically. To simplify, we have assumed that the background protons are undisturbed, i.e., the first term in the left-hand side of Equation (A1) can be neglected, which is reasonable in the limit $m_{\rm R}\gg 1$. We also consider a case where $\gamma_{\rm b}\to 1$ (a larger $\gamma_{\rm b}$ reduces the effective $n_{\rm b}/n_0$). The solutions for γ^2 for different k and $(\nu_{\rm b}/a_{\rm th,e})$ are displayed in Figure 10. The figure indicates that the mode corresponding to the fastest growth rate is $k\approx\omega_{\rm pe}/\nu_{\rm b}$ (Equation (3)) and the growth rate drops to zero, when $\nu_{\rm b}/a_{\rm th,e}<1$. Therefore, whenever the thermal speed of electrons is smaller than the beam velocity, the contribution from the ES mode becomes significant, which raises the electron temperature to stabilize the system, as elaborated upon in Section 6.

ORCID iDs

Siddhartha Gupta https://orcid.org/0000-0002-1030-8012 Damiano Caprioli https://orcid.org/0000-0003-0939-8775 Anatoly Spitkovsky https://orcid.org/0000-0001-9179-9054

References

```
Amato, E., & Blasi, P. 2009, MNRAS, 392, 1591
Arbutina, B., & Zeković, V. 2021, APh, 127, 102546
Axford, W. I., Leer, E., & Skadron, G. 1977, ICRC (Budapest), 11, 132
Bell, A. R. 1978, MNRAS, 182, 147
Bell, A. R. 2004, MNRAS, 353, 550
Bell, A. R., Schure, K. M., Reville, B., & Giacinti, G. 2013, MNRAS, 431, 415
Blandford, R. D., & Ostriker, J. P. 1978, ApJL, 221, L29
Bohdan, A., Niemiec, J., Pohl, M., et al. 2019, ApJ, 878, 5
Bohdan, A., Weidl, M. S., Morris, P. J., & Pohl, M. 2022, PhPl, 29, 052301
Bret, A., & Dieckmann, M. E. 2010, PhPl, 17, 032109
Caprioli, D., Haggerty, C. C., & Blasi, P. 2020, ApJ, 905, 2
Caprioli, D., Pop, A., & Spitkovsky, A. 2015, ApJL, 798, 28
Caprioli, D., & Spitkovsky, A. 2014a, ApJ, 783, 91
Caprioli, D., & Spitkovsky, A. 2014b, ApJ, 794, 46
Crumley, P., Caprioli, D., Markoff, S., & Spitkovsky, A. 2019, MNRAS,
  485, 5105
Giacalone, J., Burgess, D., Schwartz, S. J., & Ellison, D. C. 1993, ApJ,
  402, 550
Guo, X., Sironi, L., & Narayan, R. 2014a, ApJ, 794, 153
Guo, X., Sironi, L., & Narayan, R. 2014b, ApJ, 797, 47
```

```
Gupta, S., Caprioli, D., & Haggerty, C. 2022, ICRC (Berlin), 484
Gupta, S., Caprioli, D., & Haggerty, C. C. 2021, ApJ, 923, 208
Haggerty, C. C., & Caprioli, D. 2020, ApJ, 905, 1
Hoshino, M., & Shimada, N. 2002, ApJ, 572, 880
Kumar, N., & Reville, B. 2021, ApJL, 921, L14
Lee, R. E., Chapman, S. C., & Dendy, R. O. 2004, ApJ, 604, 187
Morlino, G., Amato, E., Blasi, P., & Caprioli, D. 2010, MNRAS, 405, L21
Morris, P. J., Bohdan, A., Weidl, M. S., & Pohl, M. 2022, ApJ, 931, 129
Muschietti, L., & Lembège, B. 2017, AnGeo, 35, 1093
Orusa, L., & Caprioli, D. 2023, PhRvL, 131, 095201
Park, J., Caprioli, D., & Spitkovsky, A. 2015, PhRvL, 114, 085003
Riquelme, M. A., & Spitkovsky, A. 2009, ApJ, 694, 626
```

```
Shalaby, M., Lemmerz, R., Thomas, T., & Pfrommer, C. 2022, ApJ, 932, 86 Sironi, L., Spitkovsky, A., & Arons, J. 2013, ApJ, 771, 54 Spitkovsky, A. 2005, in AIP Conf. Ser. 801, Astrophysical Sources of High
```

Energy Particles and Radiation, ed. T. Bulik, B. Rudak, & G. Madejski (Melville, NY: AIP), 345

Thomas, V. A., Winske, D., & Omidi, N. 1990, JGR, 95, 18809 Treumann, R. A. 2009, A&ARV, 17, 409

Wilson, L. B., Sibeck, D. G., Turner, D. L., et al. 2016, PhRvL, 117, 215101 Xu, R., Spitkovsky, A., & Caprioli, D. 2020, ApJL, 897, L41

Zacharegkas, G., Caprioli, D., Haggerty, C., Gupta, S., & Schroer, B. 2022, ApJ, 967, 71

Zweibel, E. G., & Everett, J. E. 2010, ApJ, 709, 1412